Biophysical Journal Volume 65 November 1993 2201-2216

Torque Generated by the Flagellar Motor of *Escherichia coli*

Howard C. Berg and Linda Turner
Rowland Institute for Science, and Department of Cellular and Developmental Biology, Harvard University, Cambridge, Massachusetts, USA

ABSTRACT Cells of the bacterium *Escherichia coli* were tethered and spun in a high-frequency rotating electric field at a series of discrete field strengths. This was done first at low field strengths, then at field strengths generating speeds high enough to disrupt motor function, and finally at low field strengths. Comparison of the initial and final speed versus applied-torque plots yielded relative motor torque. For backward rotation, motor torque rose steeply at speeds close to zero, peaking, on average, at about 2.2 times the stall torque. For forward rotation, motor torque remained approximately constant up to speeds of about 60% of the zero-torque speed. Then the torque dropped linearly with speed, crossed zero, and reached a minimum, on average, at about −1.7 times the stall torque. The zero-torque speed increased with temperature (about 90 Hz at 11°C, 140 Hz at 16°C, and 290 Hz at 23°C), while other parameters remained approximately constant. Sometimes the motor slipped at either extreme (delivered constant torque over a range of speeds), but eventually it broke. Similar results were obtained whether motors broke catastrophically (suddenly and completely) or progressively or were de-energized by brief treatment with an uncoupler. These results are consistent with a tightly coupled ratchet mechanism, provided that elastic deformation of force-generating elements is limited by a stop and that mechanical components yield at high applied torques.

INTRODUCTION

A bacterial flagellum is driven at its base by a reversible rotary motor, the power input of which is determined by proton motive force and proton flux and power output by torque and speed. Interrelationships between these parameters provide important constraints on motor mechanisms. For recent reviews on flagellar structure and function, see Jones and Aizawa (1991) and Macnab (1992). The rotational speed of a cell tethered to glass by a single flagellum is proportional to proton motive force, at least up to a value of −80 mV (Manson et al., 1980; Ravid and Eisenbach, 1984; Conley and Berg, 1984; Khan et al., 1985) and possibly beyond (Khan et al., 1990). There is a small threshold for rotation as cells are energized, but not as they are de-energized (Khan et al., 1985). Changes in proton flux are proportional to changes in speed (Meister et al., 1987). At the relatively high speeds of flagellar bundles, torque drops linearly with increasing speed, and extrapolation of these data back to the low speed of a tethered cell suggests a linear torque-speed relationship (Lowe et al., 1987). In an attempt to explain these interrelationships, Meister et al. (1989) studied the dynamics of a tightly coupled motor mechanism (in which the passage of a fixed number of protons carries the motor through one revolution). This analysis generated a linear torque-speed relationship, as required. In addition, it suggested that more could be learned about the motor if it were driven backward or forward by an externally applied torque.

Our first attempt to apply torque involved the construction of a quadrupole magnet with windings that could be driven in quadrature, generating a rotating magnetic field. Microscopic magnetic needles were linked to the surface of a motile *Streptococcus* by an avidin-biotin reaction, and tethered cells were spun at relatively high speeds (Berg and Turner, unpublished observations). However, without knowing the direction of the magnetic moment and its magnitude, or the angle between the moment and the applied field, we were not able to compute the applied torque. Our second attempt involved the use of a rotating optical trap. While this method proved useful for measuring the compliance of flagellar components (Block et al., 1989, 1991), it did not allow us to spin cells at a sufficiently high speed.

An elegant solution to this problem was presented by Washizu et al. (1993), who spun tethered cells of a smooth-swimming strain of *Salmonella typhimurium* (a close relative of *Escherichia coli*) with a 0.5-MHz rotating electric field at speeds up to about 100 Hz. Electrorotation has a long history (cf. Jones, 1984), but it had not been used before with tethered bacteria; for a recent review, see Foster et al. (1992). For this application, its main advantages are (*a*) cells need not be prepared in any special way; (*b*) the applied torque is well defined (i.e., proportional to the square of the electric field strength); and (*c*) the applied torque is independent of the orientation of the tethered cell—since the field spins much more rapidly than the cell, it averages over cell orientations. We have improved on this technique by (*a*) working at higher conductivities, higher frequencies, and higher field strengths; (*b*) minimizing heating by using tungsten wire electrodes in a relatively large chamber and tethering cells to sapphire (sapphire has a much higher thermal conductivity than glass); (*c*) using bacteria that tether with high efficiency without antibody; and (*d*) covalently linking their flagellar filaments

---

Received for publication 27 May 1993 and in final form 18 August 1993.

Address reprint requests to Dr. Howard C. Berg, Cellular and Developmental Biology, Harvard University, 16 Divinity Avenue, Cambridge, MA 02138-2020.

Abbreviations used: CCW, counterclockwise; CW, clockwise; DMSO, dimethylsulfoxide; DNP, 2,4-dinitrophenol; FCCP, trifluoromethoxycarbonyl-cyanide phenylhydrazone; HSAB, *N*-hydroxysuccinimidyl-4-azidobenzoate; TES, *N*-tris[hydroxymethyl]methyl-2-aminoethanesulfonic acid.

0006-3495/93/11/2201/16 $2.00

to the substratum. Most of our data were obtained with cells of *E. coli* deleted for *cheY* that spin exclusively counterclockwise (CCW); some were obtained with wild-type cells that spin predominantly CCW.

Whereas Washizu et al. (1993) concluded that motor torque is constant up to about 100 Hz for rotation in either direction, we find that it is constant up to this speed (at room temperature) only for forward (CCW) rotation. There is a substantial barrier resisting backward (clockwise, CW) rotation. At higher speeds CCW, the torque drops linearly with speed to zero and beyond. These results are consistent with our earlier data but not with their linear extrapolation (Lowe et al., 1987). The tightly coupled mechanism of Meister et al. (1989) can account for the barrier resisting CW rotation but not for the CCW constant-torque plateau, unless the displacement of a force-generating element is limited by a stop.

MATERIALS AND METHODS

Chemicals

Chemicals were obtained from the following sources: BDH Chemicals, Ltd. (Poole, England), sodium dodecyl sulfate (specially pure); Difco Laboratories, Inc. (Detroit, MI), bacto tryptone; E. I. Dupont de Nemours and Co., Inc. (Wilmington, DE), trifluoromethoxycarbonyl-cyanide phenylhydrazone (FCCP); Hüls America, Inc. (Bristol, PA), 4-aminobutyldimethylmethoxysilane; Ladd Research Industries, Inc. (Burlington, VT), 1,1,2-trichloro-1,2,2-trifluoroethane (Freon 113) and silicon monoxide crystals (99.9% pure); Pierce (Rockford, IL), *N*-hydroxysuccinimidyl-4-azidobenzoate (HSAB); Sigma Chemical Co. (St. Louis, MO), ampicillin sodium salt, dimethyl sulfoxide (DMSO), 2,4-dinitrophenol (DNP), dipotassium salt of EDTA, formaldehyde 37%, kanamycin monosulfate, stearic acid butyl ester, tetracycline-HCl, and *N*-tris[hydroxymethyl]methyl-2-aminoethanesulfonic acid (TES, pK 7.4). Other chemicals were reagent grade. Water was deionized (18 MΩ-cm) and filtered (0.2 μm). Conductivities were measured in a 1-cm^3 cell (conductivity meter CDH70; Omega Engineering, Inc., Stamford, CT) calibrated with a standard solution of KCl (10 mM).

Cells

We studied two strains of *E. coli* K12, both derived from a strain wild type for chemotaxis, AW405 (Armstrong et al., 1967). Both were constructed by Karen Fahrner (K. A. Fahrner and H. C. Berg, manuscript in preparation). Their flagellar filament protein is specified by plasmid pFD313 (*amp*^{R}, a derivative of pBR322, kindly supplied by Goro Kuwajima) (Kuwajima, 1988) and is deleted for amino acids 245–301. The chromosomal gene carries the *fliC726* allele, with a nonflagellate phenotype (Silverman and Simon, 1973). The filaments specified by the plasmid adhere spontaneously to many surfaces (glass coverslips out of the box, silanized glass, etc.), so both strains are easy to tether without the use of anti-filament antibody. Strain KAF84 is wild-type for chemotaxis and carries a *zeb741*::Tn*10* marker. It also lacks pili (is *pilA'-kan*) (Maurer and Orndorff, 1987). Strain KAF95 carries a *cheY* deletion (m43-10, from strain RP4979, the gift of Sandy Parkinson) and, thus, swims smoothly (rotates its flagella exclusively CCW).

Preparation of cells

Cultures were inoculated from reference stocks and grown to saturation in tryptone broth (1% tryptone, 0.5% NaCl) containing the requisite antibiotics at 30°C (ampicillin, kanamycin, and/or tetracycline at 100, 40, or 12 μg/ml, respectively). DMSO was added (10% v/v) and 0.1-ml aliquots were frozen at –75°C. These aliquots were thawed as needed, added to 10 ml of the original medium, and grown to saturation. This culture was diluted 1:20 with fresh medium and incubated for another 4 h. Cells were harvested by centrifugation at 2200 × *g* for 7 min at room temperature. The pellet was resuspended in 1.5 ml 10 mM potassium phosphate (pH 7.0) and 0.1 mM EDTA (motility medium). Most of the flagellar filaments were sheared off by passing the suspension back and forth 25 times between two syringes with 26-gauge needles connected by a piece of polyethylene tubing (12 cm long, 0.58 mm inner diameter). The filaments were separated from the cells by performing centrifugation and resuspension twice. The final suspension was diluted in motility medium to 1.5 times the original volume (approximately 10^8 cells/ml).

Tethering

Sapphire windows were baked in air for 8 h at 900°C (to remove any residual silane). They were then coated with about 30 nm of silicon monoxide under vacuum in a Denton evaporator (model DV-502; Denton Vacuum, Inc., Cherry Hill, NJ) following the procedure of Bradley (1965). A 1% solution of 4-aminobutyldimethylmethoxy silane in 95% ethanol was allowed to stand at room temperature for 3 min (to hydrolyze the methoxy groups). The sapphire windows were dipped into this solution for 15 s, rinsed gently by dipping in 95% ethanol, placed silicon side up on a clean microscope slide, and baked in air for 12 min at 110°C (to drive off water and to complete the formation of silicon-oxygen bonds). The windows were cooled and secured coated side up with Apiezon M grease (Apiezon Products, London) in delrin holders (comprising the bottom part of the flow cell assembly, described below).

It was not possible to spin tethered cells at high speed unless their flagellar filaments were covalently linked to the surface. To accomplish this, we modified the amino groups of the silane with a heterobifunctional photoreactive cross-linker HSAB. All subsequent procedures were carried out in the dark or under a red safe light. A stock solution of HSAB (25 mM in DMSO) was diluted 1:50 in 10 mM sodium phosphate (pH 8.0) and layered over the silanized surface (about 0.25 ml per window). The windows were put in a humidity chamber at room temperature for 15 min (to allow time for acylation of the amino groups). Then the windows were rinsed by tilting the holders and pouring the following solutions across the surface: 10 mM sodium phosphate, pH 8.0; 10% aqueous DMSO (to dissolve HSAB crystals that might remain); 10 mM sodium phosphate, pH 8.0; 1% aqueous formaldehyde (to block unreacted amino groups); 10 mM sodium phosphate, pH 8.0; and, finally, 10 mM potassium phosphate, pH 7.0, 0.1 mM EDTA (the motility medium). Small flow cells were constructed by covering each window with a 12-mm diameter glass coverslip to which two supports had been cemented (each made from a one-third-round piece of a silicon-rubber gasket (SX00 013 01; Millipore Corporation, Bedford, MA).

Under a safe light, approximately 0.1 ml of the cell suspension (see above) was added to each chamber and allowed to stand for 5 min (long enough for the flagellar stubs of strain KAF84 or KAF95 to tether spontaneously). The free cells were rinsed away with about 1.5 ml of the motility medium (added to one side of the flow cell with a dropper and wicked away at the opposite side with a piece of filter paper). The aryl azide of HSAB was activated by a near-UV flash (70 watt-s generated by a xenon lamp mounted at one focus of an ellipsoidal reflector, as described by Shimada and Berg, 1987). Finally, the buffer rinse was repeated. The holders were stored in a humidity chamber in room light at room temperature until used for the day's experiments. Just before the flow cell was assembled, the window was rinsed with the buffer to be used in the experiment, and the coverslip was removed.

At the end of the day, the silicon-monoxide coating was removed by gently rubbing the window over a flat surface covered with a polishing cloth impregnated with 1 μm diamond dust in a petroleum distillate (components supplied by Buehler, Ltd., Lake Bluff, IL). Then the windows were rinsed with heptane, sonicated in a household detergent (Mr. Clean), sonicated in hot water, dried under a heat lamp, and sonicated in 1,1,2-trichloro-1,2,2-trifluoroethane. Finally, they were returned to the baking oven (i.e., recycled to the beginning of the tethering procedure).

Data acquisition

The rotation of tethered cells was monitored with a linear-graded filter apparatus (Kobayasi et al., 1977; Berg et al., 1982). Light emerging at the camera tube of a phase-contrast microscope was split into two beams (Fig. 1). Each beam was imaged by an eyepiece onto the surface of a linear-graded filter (Fig. 2). The filters were set at right angles to one another. Each has a linear transmission gradient, so that the intensity of the transmitted light is proportional to the x- or y-weighted integral of the image-intensity distribution. As a consequence, a tethered bacterium, rotating about a fixed point at a constant speed, produces pure cosine and sine signals, regardless of the shape of the image. Our filters were made by evaporating a metallic film (Inconel 600) (Goodell, 1973) onto a glass substrate, with the required spatial variation produced by the motion of a computer-controlled baffle in the path of the metallic beam. The photomultiplier outputs were fed via current-to-voltage converters (10^8 Ω feedback) to operational amplifiers that removed the DC offset and then to adjustable two-pole passive RC filters. The x and y signals from the filters were digitized in a 16-bit analogue-to-digital converter (NB-MIO-16X, with NB-DMA2800 direct memory access; National Instruments, Austin, TX), sampled on-line by a minicomputer (Macintosh Quadra 900, using National Instruments LabView 2.2 software), and streamed to disk. Data were acquired in blocks of 2 × 1024 points at rates of 500, 1000, or 2000 x, y pairs/s. The filter time constant was set equal to the sampling interval.

Data reduction

Fig. 3 shows options developed for analyzing the data. We looked directly at the x or y signals generated by the linear-graded filters (Fig 3, *top*). Or we offset and scaled each data set to the range ± 1 (to represent cos θ and sin θ, where θ is the angle of orientation of the cell), computed $\theta = \arctan(\sin\theta/\cos\theta)$, unwrapped the phase, and displayed θ as a function of time (Fig. 3, *middle*). Alternatively, we passed the cos θ or sin θ data set through a Hann filter (to reduce leakage due to abrupt transitions at the beginning and end of the set) and computed the power spectrum. We did this for cos θ and sin θ separately and then summed the result (Fig. 3, *bottom*). In the experiment shown, the cell was driven backward (CW). It started spinning at about 31 Hz, then abruptly sped up to about 43 Hz; the motor broke (see below). This transition appeared in the (θ, t) plot as a change in slope (Fig. 3, *middle*) and generated a second spectral peak (*bottom*). Most spectra had a single, sharp, symmetric peak, and we simply read off the frequency at its maximum. Spectral analysis proved more convenient than line fits to (θ, t) plots, because cells often hesitated (stuck briefly to the sapphire surface?). This generated (θ, t) plots with embedded short horizontal segments, which required individually tailored multiple line fits. Spectral analysis also had the advantage that the image of a cell could be moved to the edge of the linear-graded filters, so that the signals cycled up and down as more or less of the image was visible. This gave larger modulations; however, (θ, t) plots could not be made, because the x and y signals were now in phase, rather than 90° out of phase.

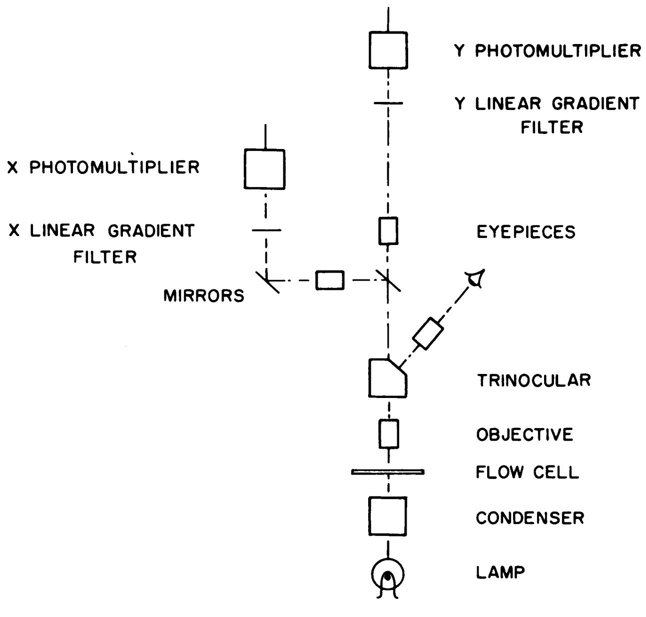

FIGURE 1 Linear-graded filter apparatus. Lamp: 100-watt Xenophot (Osram HLX 64625) driven by a regulated DC power supply. Condenser: Nikon (Melville, NY) S-Ke phase contrast. Flow cell: see Fig. 5. Objective: Nikon CF Plan 20× BM. Not shown: Zeiss (Thornwood, NY) Optovar, magnification 1.6. Trinocular: Nikon S-Ke, 100% visual, 100% photo, magnification 1.25. Eyepieces: 20× (surplus). Linear-graded filters: see Fig. 2. Photomultipliers: RCA C7164R (red-sensitive multialkali; now made by Richardson Electronics, Ltd., Chicago, IL).

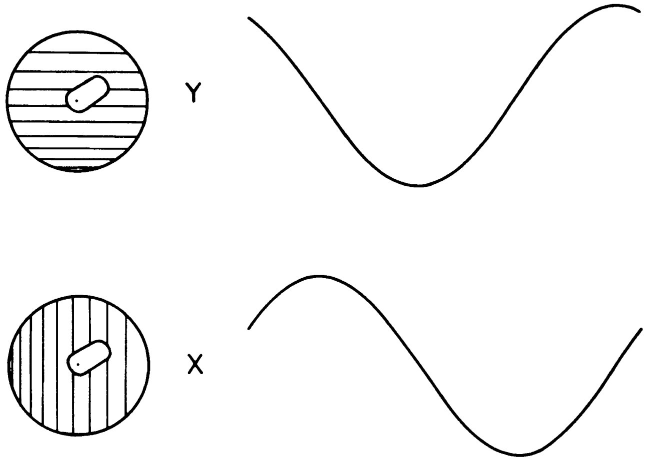

FIGURE 2 (*Left*) x and y linear-graded filters (4-mm diameter) viewed from above, showing the image of a tethered cell. The transmission of the x filter increases linearly from left to right, and the transmission of the y filter increases linearly from bottom to top (both from 16% to 89%). (*Right*) intensity of transmitted light obtained when the image rotates at a constant speed one revolution clockwise.

Electrodes

Seven epoxy-insulated tungsten microelectrodes (0.13 mm diameter) with 12° tapered tips (no. 5772; A-M Systems, Everett, WA) were sealed with burgundy pitch (melting point 80°C) into a 0.4-mm-diameter hole drilled through a brass plate, so that 0.12 mm at the tip projected beyond the surface of the brass. The projecting material was removed with silicon-carbide lapping paper (M-600 grit). Then the electrodes were cut to length (1.4 cm) and freed by soaking in chloroform. Finally, 0.4 cm of the insulation at the back end was removed with a razor blade. Four of these wires were clamped into small insulated brass electrode holders with opposed 0–80 brass screws. One screw of each pair was soldered to the center wire of a coaxial cable connected to the oscillator (see below). The electrodes angled downward (declination 6°) so that their truncated tips met near the optical axis of the objective, as shown in Fig. 4. At the end of a day's experiments, the electrodes were rinsed with water, wicked dry, and left in air. Every month or so, they were soaked for a few minutes in 2% (w/v) sodium dodecyl sulfate (to remove adherent bacteria).

Oscillator

The oscillator used to power the electrodes was computer controlled, with 12-bit digital-to-analogue lines setting its frequency and amplitude, and digital lines selecting the direction of rotation and gating the output. The

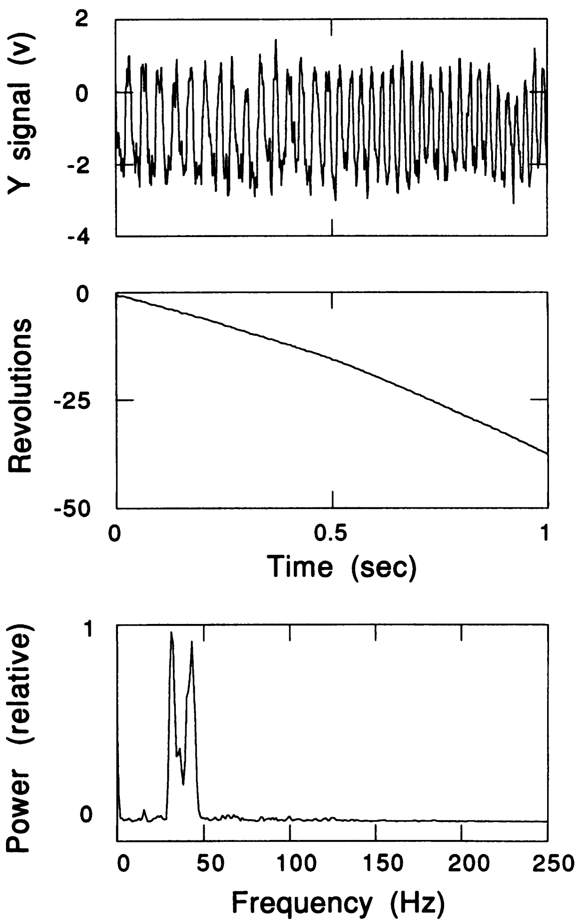

FIGURE 3 Data reduction. (*Top*) raw data (channel *y*; 1000 of 1024 points are shown). (*Middle*) angle of cell orientation (in revolutions) as a function of time. (*Bottom*) summed power spectrum for channels *x* and *y* (truncated, original to 512 Hz). There are two peaks here, not because the spectra for the two channels were different, but because the cell changed its speed halfway through the time interval sampled.

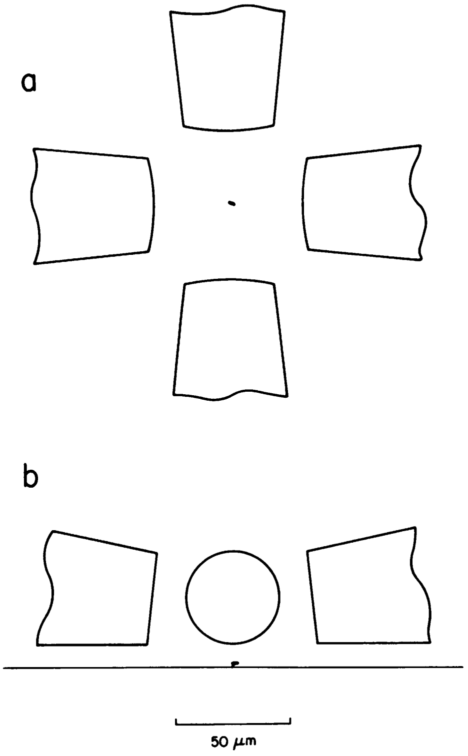

FIGURE 4 Tips of the tungsten wire microelectrodes. (*a*) top view; (*b*) side view. The tips were about 40 μm across, 70 μm apart (face to face), and 10 μm away from the surface of the sapphire window. A tethered cell is shown to scale near the optical axis.

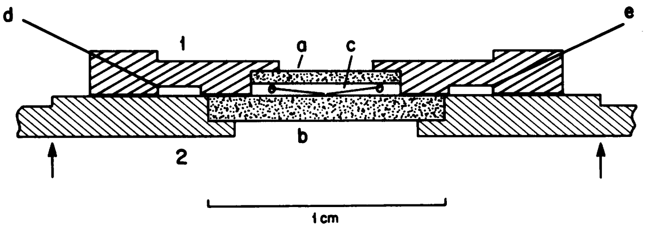

FIGURE 5 Scale drawing of the flow-cell electrode assembly. (*1*) upper part (gold-plated brass), mounted rigidly on the microscope objective (not shown). (*2*) lower part (black delrin), mounted on an *x*, *y* stage (not shown). Arrows indicate direction of spring loading. (*a*) glass window (cut from a hemacytometer coverslip; sapphire cannot be used here because it is birefringent and would generate double images). (*b*) sapphire window, to which cells were tethered (10-mm diameter, 1 mm thick, model 02WSA004; Melles Griot, Irvine, CA). (*c*) tungsten wire electrodes (Fig. 4). (*d, e*) stainless steel tubes (22-gauge) for fluid transfer.

oscillator was built around a direct digital synthesizer (no. 1172; Stanford Telecom, Santa Clara, CA) that generated two 8-bit words at the rate of 32 MHz, one word defining sin ωt, the other cos ωt. These words were converted to analogue form, and the analogue signals were passed through amplitude control circuitry and used to drive two 75-W wideband push-pull amplifiers. Each amplifier, in turn, was connected to the input windings of a wideband transformer (with a switch-selectable turns ratio of 1:2 or 1:4, defining low-power or high-power output scales, respectively). Each output winding (center tap grounded) was connected to an electrode pair with two coaxial cables. The electrode pairs were driven in quadrature. With the oscillator set at 100% on the low-power scale, the peak-to-peak potential difference between electrodes of each pair was about 115 V. We did not accurately calibrate the difference in power levels between the high-power and low-power scales; it was not 4, as might be expected from the output transformer turns ratios, but closer to 5, as measured by the ratio of rotation rates of cells spun at both low- and high-power settings. This difference was due to a range-dependent shift in the resonance frequency of the output circuit.

Flow cell

The flow cell was made in two parts (Fig. 5). The upper part (part 1) was mounted rigidly on the phase-contrast objective and centered on its optical axis. The lower part (part 2), comprising a holder for the sapphire window to which cells were tethered, was fixed via four spring-loaded pins to an *x*, *y* stage (not shown; adjusted by micrometer screws). The pins constrained the lower part to follow the horizontal displacements of the stage, while the springs forced it upward (as shown by the arrows), so that it remained in close contact with part 1. The space between the windows was filled with a motility medium. The medium could be changed by pumping fluid in and out of two stainless-steel tubes (Fig. 5, *d* and *e*, respectively). The fluid passed from each tube to the center of the cell by moving through a thick transverse and a thin longitudinal channel. The transverse channel acts as a constant-pressure source that feeds fluid into the longitudinal channel along its entire width (Berg and Block, 1984). In the present application, fluid was forced in under positive pressure with a syringe pump (model 22; Harvard Apparatus, South Natick, MA) run at 20 ml/h so that fluid leaked slowly out (rather than air in) through the gap between parts 1 and 2. The excess fluid was removed by blotting with pieces of filter paper. The electrodes (Fig. 5, *c*) entered the chamber as a quadrupole array, offset 45° from the longitudinal axis of the flow cell. Two of the four electrodes are shown in Fig. 5, emerging from holes drilled through part 1 (~0.5-mm diameter, sealed with silicone rubber). The other end of each electrode was held by an insulated clamp mounted on the assembly (not shown) that fixed part 1 to the objective. The objective was thermally and electrically insulated from the nose piece of the microscope with a delrin sleeve and cooled by a heat exchanger near the top with water from a refrigerating circulator (Lauda RMS-6; Brinkmann Instruments, Inc., Westbury, NY). The *x, y* stage also was cooled, but not as effectively. The temperature at the edge of the sapphire window was measured under conditions similar to those of the experiments with a small thermistor (GB31J1; Fenwal Electronics, Inc., Milford, MA) calibrated with a mercury thermometer traceable to the National Bureau of Standards. When the circulator was set at 9.0, 15.0, or 22.0°C, the temperature at the edge of the sapphire window was 11.2, 16.2, or 22.6°C, respectively. The latter temperatures were probably accurate to within 0.2°C, but it would have been better to have controlled the temperature of the flow cell directly.

RESULTS

Choice of buffer

We began with the assumption that joule heating might be prohibitive, so we chose a buffer with a low conductivity (1 mM potassium phosphate, pH 7.2, 0.1 mM EDTA, conductivity 0.19 mS/cm). Later, we found that larger applied torques were generated in media of higher conductivity (e.g., 40 mM TES, pH 7.0, 0.1 mM EDTA, conductivity 0.41 mS/cm). Fig. 6 shows rotational speeds for tethered cells in a series of different buffers. At low conductivities (1 mM TES, pH 6.0, 0.004 mS/cm, and 1 mM TES, pH 7.0, 0.037 mS/cm) the cells spun in the same direction as the electric field (plotted at positive speeds; Fig. 6). At an intermediate conductivity (4 mM TES, pH 7.0, 0.088 mS/cm) some cells spun one way, some spun the other, but most stopped (data not shown). At higher conductivities, the cells spun in the opposite direction (plotted as negative speeds; Fig. 5). Sodium phosphate, which fell on the same curve as TES, was more effective at higher conductivities than potassium phosphate. Also, TES buffers at the same (high) conductivity were more effective at pH 6 than at pH 7 (data not shown).

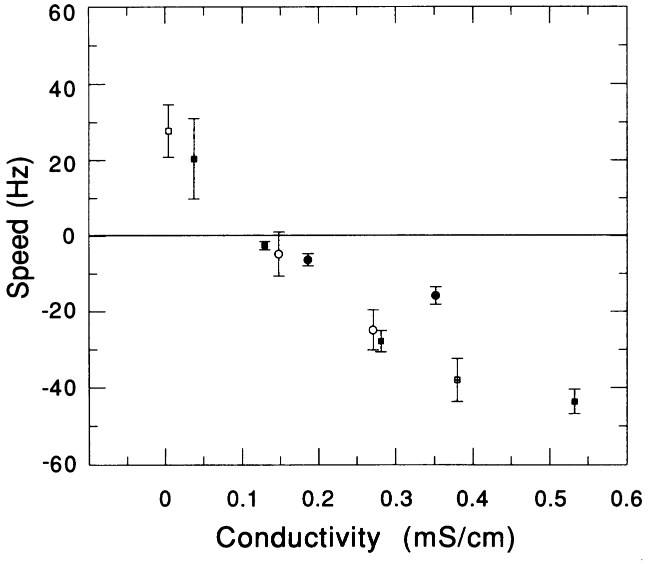

FIGURE 6 Rotational speed as a function of conductivity (positive in the direction of rotation of the applied field). The error bars are SEs for the cell population. If cells spun under their own power, the speed shown is the increment generated by the applied torque (20% power on the low-power scale, 2.25 MHz). All buffers contained 0.1 mM EDTA. □, 1 mM TES, pH 6.0; ■, 1 to 50 mM TES, pH 7.0; ○, 1 or 2 mM sodium phosphate, pH 7.2; ⊞, 25 mM TES + 1 mM sodium phosphate, pH 7.0; ●, 1 or 2 mM potassium phosphate, pH 7.2. Measurements made at room temperature (~24°C).

In our early experiments (in 1 mM potassium or sodium phosphate, pH 7.2), free cells tended to accumulate at the tips of the electrodes. At higher conductivities (e.g., in 40 mM TES, pH 7.0) they did not. In either case, the field appeared to stir the medium; free cells moved in arcs near the tips of the electrodes. This motion was more vigorous at higher power. When working in 1 mM potassium or sodium phosphate, we noted a distressing artifact: when the field was turned on, cells spun more rapidly for the first few tenths of a second than they did later on. This transient had a smaller amplitude but was longer lived at lower power. Also, this effect was smaller when buffer was pumped through the flow cell. We suspect that this artifact was due to elevated conductivity near the tips of the electrodes arising from leakage of ions from cells that had accumulated there. If this were so, field-induced stirring or buffer flow would reduce the conductivity to the value of the bulk medium, decreasing the applied torque (Fig. 6). This problem was not apparent in 40 mM TES (pH 7.0), where cells spun at constant speed. Since cells also spun vigorously for many hours on their own in this buffer, we chose it for subsequent work.

Choice of frequency

We selected two buffers, one at low conductivity and the other at high conductivity, and studied the variation in speed with frequency of the applied electric field (Fig. 7). At high conductivity, the response peaked at about 1.5 MHz; at low conductivity, it peaked at about 0.75 MHz. Both curves were relatively broad. Since the buffer of high conductivity was preferred (see above), we chose to work at 2.25 MHz, where the waveforms showed low distortion on both low- and high-power scales.

Heating and electrical damage

We tethered cells to sapphire, because sapphire has a thermal conductivity 20 to 30 times higher than that of glass (depending on glass type). The temperature rise generated by current flowing between the electrodes was estimated by coating the sapphire window (as modified for tethering) with stearic acid butyl ester (melting point on our scale ~26.9°C), setting the temperature of the window at 26.4°C, and measuring the power level required to melt particles of different size. In 40 mM TES (pH 7.0), 0.1 mM EDTA, bits of this wax in the center of the field that were about 16 μm in diameter just melted (were heated~ 0.5°C) at 40% on the

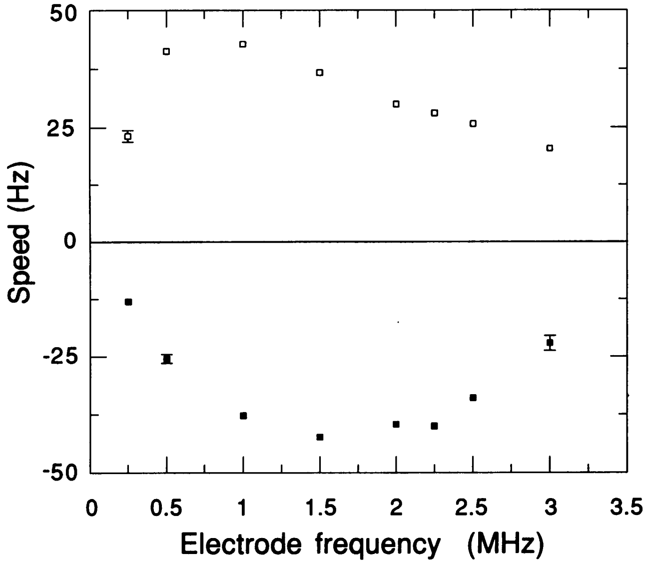

FIGURE 7 Rotational speed as a function of the frequency of the applied electric field. (*Top*) □, 3 cells in 1 mM TES, pH 6.0, 0.004 mS/cm. (*Bottom*) ■, 5 cells in 40 mM TES, pH 7.0, 0.41 mS/cm. The data for each cell were corrected for frequency-dependent variations in field amplitude (measured with an oscilloscope using high-impedance probes) and normalized to the mean speed over the cell ensemble at 2.25 MHz. The error bars are the SEs for each normalized data set (not shown if smaller than the symbols). None of these cells spun under their own power. Measurements were made at room temperature (~24°C).

high-power scale (at 2.25 MHz), while pieces about 4 μm in diameter or smaller did not melt, even at 100% on the high-power scale. We conclude that objects as close to the sapphire surface as tethered *E. coli* are heated less than 0.2°C at 40% on the high-power scale (this is the highest power level used to spin cells thus far) and less than 0.1°C at 100% on the low-power scale. We also conclude that there is a sizable increase in temperature as one moves along the optical axis away from the surface of the sapphire. This is expected from the electrode geometry (Fig. 4 *b*). Evidence for electrical damage was sought in a unidirectional field by disconnecting the leads to one electrode pair and driving the other at 100% on the high-power scale. The cells between the electrodes immediately lined up along the direction of the field. However, when the field was turned off, they immediately spun at their initial rates. Although the field strength was high (nearly 40,000 V/cm), the oscillation period (~4 × 10^{-4} ms) was much smaller than the electrical time constant of the cytoplasmic membrane (~1 ms; Felle et al., 1978). So one would not expect dielectric breakdown.

Breaking motors

As we shall see, there is a substantial barrier to rotation when cells are driven backward (CW for the smooth-swimming mutant used for most of our studies). When cells were spun in this direction first or had not been spun CCW faster than the zero-torque speed (see below), this barrier was readily breached. Sometimes motors broke catastrophically; the cell suddenly spun at higher speed and then stopped spinning when the field was turned off. This was the fate of the cell used to illustrate modes of data reduction (Fig. 3). Such cells never spun again on their own. Another example is shown in Fig. 8. This cell spun CCW at 10 Hz under its own power (0 to 0.5 s), was driven CW at 4.5 Hz when the field was turned on (Fig. 8, *up arrow*; 0.5 s), then two revolutions later (between 0.9 and 1 s) spun 30 Hz until the field was turned off (Fig. 8, *down arrow*; 2.5 s), and then stopped (2.5 to 3 s). The noise on this signal is due to rotational Brownian motion. Most motors broke progressively; after cells were spun forward or backward at high speed, they spun less vigorously on their own. After a few cycles of such treatment, they stopped spinning on their own, usually altogether. If they were still able to spin slowly on their own, partial or complete recovery was common. The simplest explanation for these results is that catastrophic breaks sever the drive shaft, while progressive breaks disrupt the force-generating elements. It is known that there are at least eight of the latter operating in parallel and that defective units can be replaced (Block and Berg, 1984; Blair and Berg, 1988). Disruption of force-generating elements during rapid CCW rotation would explain why motors of such cells are more difficult to break when spun CW. Partial damage reduces the height of the barrier to CW rotation and thus the torsional load on other motor components.

As far as we could tell, the behaviors of cells broken catastrophically, broken progressively but completely, or de-energized with 1 mM DNP or 0.01 mM FCCP, were indistinguishable. Evidently, the drag due to proton pumping at zero proton motive force in an intact motor is relatively small. However, cells that had been de-energized with either uncoupler for many minutes became more difficult to turn. This behavior was seen earlier in studies with optical tweezers, where motors of both *E. coli* and a motile *Streptococcus* eventually "locked up" (Block et al., 1989). Since cells of *E. coli* deleted for *motA* and/or *motB* (genes specifying components of the force-generating elements) diffuse freely

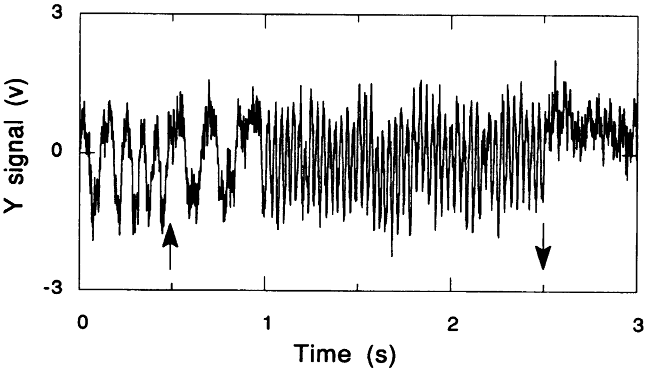

FIGURE 8 The *y* signal for an energized cell of strain KAF95, showing a catastrophic break. The electric field was turned on at 0.5 s (*up arrow*; 5% on the low-power scale) and turned off at 2.5 s (*down arrow*). Note the changes in both direction and speed (0.5 s). The catastrophic break occurred at about 0.9 s (see text). Measurements were made in 1 mM potassium phosphate, pH 7.2, 0.1 mM EDTA at room temperature (~24°C).

when tethered (Block et al., 1989), we exposed cells of such a strain (RP6665, Δ*motA*Δ*motB*, grown and tethered as described by Block et al., 1989) to 0.01 mM FCCP. These cells continued to diffuse freely (data not shown). Therefore, the increased difficulty that we observed in turning cells following prolonged treatment with an uncoupler has something to do with the way in which MotA and/or MotB interacts with the rotor.

The terminal behavior of two cells broken progressively is shown in Fig. 9. In most cases, the speed of broken cells was remarkably linear with power, up to speeds of at least 400 Hz, as evident here. In the CW direction the speed remained linear up to the highest speeds tested (980 Hz); however, in the CCW direction there was a discontinuity in slope, beyond which the cells became easier to turn (Fig. 9). We suspect a phase transition in the tether that allowed the cell to tip up or spin farther away from the sapphire surface. This discontinuity was not due to a change in applied torque, because it occurred only when cells were driven CCW. The initial slopes were often steeper in the CW than in the CCW direction, while the final slopes were more nearly the same (Fig. 9).

Determining torque as a function of speed: theory

Given that one can break (or de-energize) motors and the internal friction is small, it is possible to learn how motor torque varies with speed (cf. Washizu et al., 1993, who de-energized cells by exposure to UV light). For a cell spinning under its own power, the rotational speed is

$$s_0 = N(s_0)/2\pi f, \qquad (1)$$

where $N(s)$ is the motor torque at speed s, and f is the cell's rotational frictional drag coefficient. f is a function of cell shape, tethering geometry, and fluid viscosity. For a cell with a broken motor spinning under an externally applied torque $A(E^2)$, the rotational speed is

$$s_a = A(E^2)/2\pi f, \qquad (2)$$

where f is the same coefficient as in Eq. 1. The applied torque is a function of the square of the field strength, E, but not of the cell's speed. When both torques are applied at the same time, the net rotational speed is

$$s = [N(s) + A(E^2)]/2\pi f. \qquad (3)$$

We define a speed offset

$$s - s_a = N(s)/2\pi f, \qquad (4)$$

a quantity proportional to motor torque at speed s. In comparing different cells, variations in frictional drag coefficient can be eliminated by computing the relative torque

$$(s - s_a)/s_0 = N(s)/N(s_0). \qquad (5)$$

Determining torque as a function of speed: experiment

Figs. 10 and 11 show how we obtained the speed offset (Eq. 4). First, we applied torque to an energized cell and measured its speed, s (Fig. 10, *filled symbols*). Next, we spun the cell rapidly CW and/or CCW until the motor broke, or alternatively, we added an uncoupler and waited until the cell stopped spinning. Third, we applied torque again and measured the speed, s_a (Fig. 10, *open symbols*). Finally, we took the difference, $s - s_a$, and plotted it as a function of s (Fig. 11). This particular plot indicates sizable torque-resisting CW rotation that peaks at about 6 Hz and nearly constant torque for CCW rotation up to speeds of at least 40 Hz. This procedure failed when motors did not break completely (or nearly so). In this event, the speed offset was not computed.

Fig. 12 shows other examples of speed offsets obtained at low power. In Fig. 12 *a*, the motor slipped CW (continued to deliver high torque over a range of speeds) before breaking. In Fig. 12 *b*, it yielded more abruptly. In Fig. 12 *c*, it was de-energized with an uncoupler. In all cases, there was a substantial torque-resisting CW rotation and nearly constant torque for CCW rotation up to about 100 Hz.

At first glance, it appeared that cells resisting CW rotation stopped turning, at least at moderate speed offsets (Figs. 11, 12). Closer examination, by eye and stopwatch, revealed that such cells actually spun slowly CW. For example, a cell was studied (in 40 mM TES, pH 7.0, 0.1 mM EDTA at room temperature) that spun on its own at about 10 Hz. With applied torques of +2.5, +5.0, and +7.5% (on the low-power scale) it spun CCW about 20, 30, and 40 Hz, respectively, indicating that the power level 2.5% matched the torque gen-

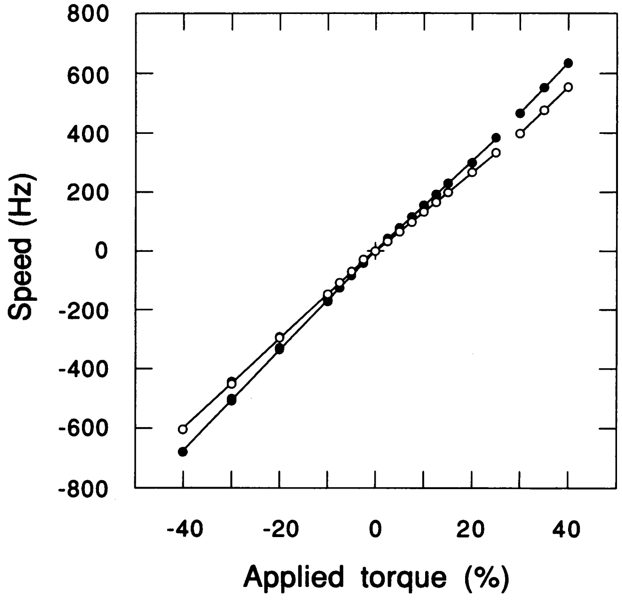

FIGURE 9 Speed as a function of applied torque for two cells broken progressively. Positive speed: CCW; negative speed: CW. Positive applied torque: a field that drives the cell CCW, expressed as percentage of full power (high-power scale). Negative applied torque: a field that drives the cell CW. Cells of strain KAF95 at 11.2°C (○) and 22.6°C (●) in 40 mM TES, pH 7.0, 0.1 mM EDTA.

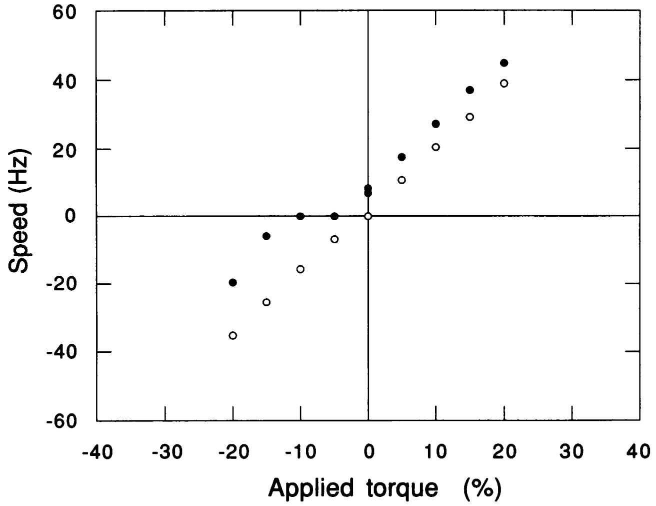

FIGURE 10 Speed as a function of applied torque. ●, data obtained with an intact motor; ○, data obtained after the motor was broken. First, the cell was spun CW and CCW with the oscillator set on the low-power scale, following the sequence 0, -5, -10, -15, -20, 0, 5, 10, 15, 20% (●, sign conventions as in Fig. 9). The 0% readings were 8.3 and 6.8 Hz, respectively. This cycle was repeated, with similar results (data not shown). The oscillator was then set on the high-power scale and the experiment was run again, yielding maximum speeds of -230 and +225 Hz (not shown); the motor broke catastrophically during the first CW interval (at -56 Hz). The oscillator was finally returned to the low-power scale, and the original cycle was repeated (○). In this case, there was still some resistance to CW rotation: the points at -5 to -20% are all a little high—when fit by a line, the line does not project back to the origin. Cells of strain KAF95 in 1 mM potassium phosphate, pH 7.2, 0.1 mM EDTA, at ~32°C. Speed transients observed with this buffer (see Choice of buffer) were minimized by waiting 0.2 s after the field was changed before data were collected.

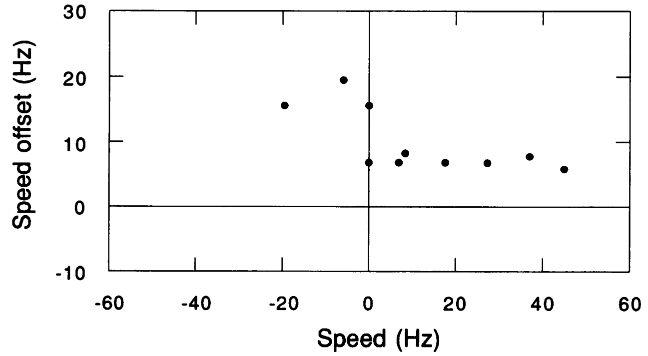

FIGURE 11 Speed offset for the data of Fig. 10. The ordinate is a number proportional to the torque generated by the flagellar motor (+ for CCW, - for CW) at the speed indicated on the abscissa (+ for CCW, - for CW); see Eq. 4. The pair of points near (7, 7) and (8, 8) were obtained at 0 applied field.

erated when the cell spun on its own. However, with applied torques of -2.5, -5.0, and -7.5%, the cell spun CW at 0.0014, 0.012, and 0.091 Hz, respectively. The corresponding speed offsets would have been 10, 20, and 30 Hz, respectively. So this cell, while resisting an applied torque three times larger than the torque generated when the cell spun on its own, spun at about 0.1 Hz. With smaller applied torques, it spun more slowly.

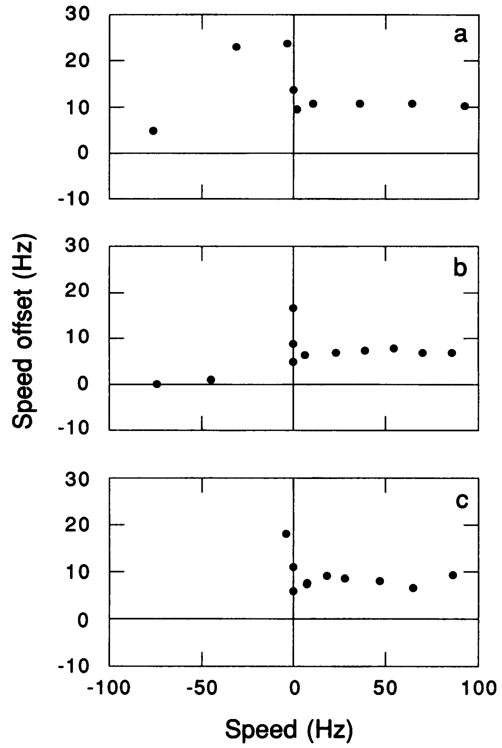

FIGURE 12 Other examples of speed offsets obtained on the low-power scale. (*a*) a cell spun CCW first up to +30% and then CW to -30%. The motor broke catastrophically while driven at -20%; data for this segment are shown in Fig. 3. In 1 mM potassium phosphate, pH 7.2, 0.1 mM EDTA. (*b*) a cell spun CCW first up to +50% and then CW to -50%. The motor broke progressively. In 40 mM TES, pH 7.0, 0.1 mM EDTA. (*c*) a cell spun CCW first up to +40% and then CW to -10%. The motor was de-energized with 1 mM DNP. TES buffer, as above. All cells: strain KAF95 at room temperature (~24°C).

We were puzzled by constant torque for CCW rotation up to about 100 Hz (Fig. 12), because we had grown accustomed to the idea, born of work with a motile *Streptococcus* (Lowe et al., 1987), that the zero-torque speed of flagellar motors at room temperature was on the order of 100 Hz. However, work on *E. coli* grown on a rich medium had suggested a much higher figure, particularly at higher temperatures (Lowe et al., 1987). Two routes for reaching zero-torque speed became apparent: (*a*) cool the cells and (*b*) just spin them faster. Both methods worked (Figs. 13 and 14). Fig. 13 *a* shows the speed offset for a cell cooled to 11.2°C and driven CCW and then CW. Going CCW, the torque was constant up to about 60 Hz, then it dropped more or less linearly, falling to zero at about 100 Hz. Going CW, a large barrier was encountered and then breached. Fig. 13 *b* shows the speed offset for a cell cooled to 16.2°C and spun in a similar manner. Going CCW, the torque was constant up to about 70 Hz, then it dropped linearly, reaching zero at about 130 Hz. Going CW, a large barrier was encountered, as before, and was soon breached. Both of these motors broke catastrophically. Fig. 14 *a* shows a cell spun at 11.2°C up to a frequency of about 550 Hz, and Fig. 14, *b* and *c*, shows cells spun at 22.6°C up to frequencies beyond 600 Hz. In these experiments, the motors showed approximately constant

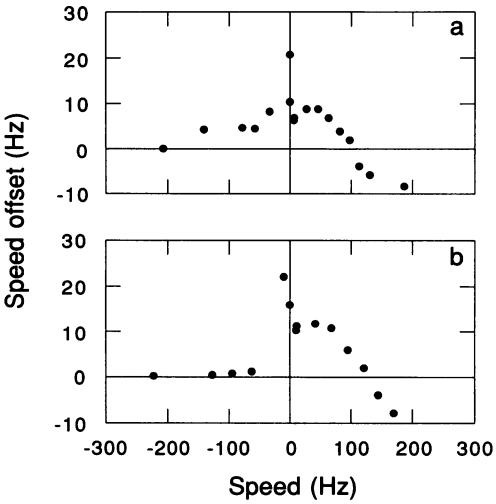

FIGURE 13 Speed offsets for two cells spun at low temperature. (*a*) 11.2°C; (*b*) 16.2°C. Cells were spun CCW up to +70% then CW up to −100% on the low-power scale. The motors of both cells broke catastrophically. Strain KAF95 in 40 mM TES, pH 7.0, 0.1 mM EDTA.

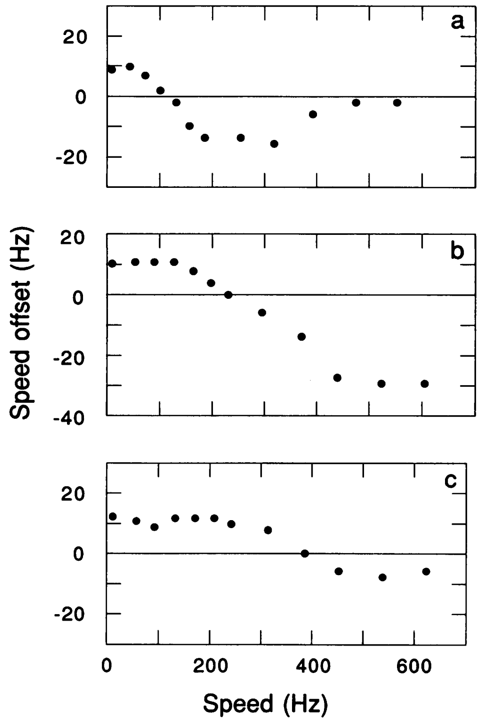

FIGURE 14 Speed offsets for cells spun at high speed. (*a*) 11.2°C; (*b* and *c*) 22.6°C. Cells were spun up to ±40% on the high-power scale. Only CCW data are shown, because motors were badly damaged going CCW (especially in *a*, where the motor was broken completely after the first CCW sequence). Rotation speeds for cells *a* and *b* observed after this damage are shown in Fig. 9. Strain KAF95 in 40 mM TES, pH 7.0, 0.1 mM EDTA.

torque up to an intermediate frequency, a linear drop in torque through zero torque and beyond, and slip at a fixed negative torque. In Fig. 14 *a* and possibly *c*, loss of torque was evident at the highest frequencies.

The same general behavior was observed with wild-type cells (Fig. 15). Cell *a* shows a particularly large CW barrier with slip. Cell *b* shows a smaller CW barrier that is more readily breached. Wild-type cells spent most of their time in the CCW mode, because joule heating, although small (see above), was large enough to trigger a CCW thermal response (Maeda et al., 1976). However, these cells occasionally tried to spin CW. When this happened, the speed changed by the amount expected were the motor to exert the same torque (except for sign) spinning in either direction. For example, a wild-type cell similar to the cell shown in Fig. 10, when subjected to torque +10%, would spin at 27 Hz CCW and then suddenly stop. When subjected to torque +20%, it would spin at 45 Hz CCW and then suddenly slow to 20 Hz CCW. Whether driven CCW or CW, a wild-type cell would switch from the behavior expected were the torques applied in the same direction to the behavior expected were the torques applied in opposite directions. These data, although limited, suggest that the torque-speed relationship for motors in wild-type cells is similar to that for motors in a *cheY* deletion strain.

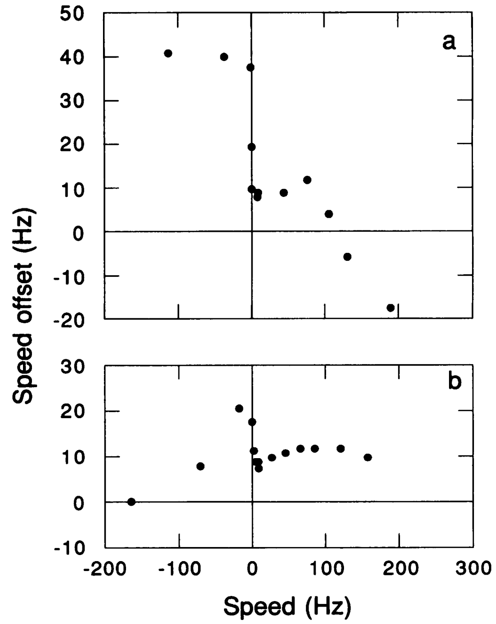

FIGURE 15 Speed offsets for wild-type cells at 16.2°C, driven up to ±80% on the low-power scale. (*a*) broken progressively; (*b*) de-energized with FCCP. Strain KAF84 in 40 mM TES, pH 7.0, 0.1 mM EDTA.

As evident from Figs. 11–15, not every feature of the torque-speed relationship could be established in a single experiment. To find the zero-torque speed, for example, it was necessary to spin the cells rapidly CCW. On the other hand, to probe the CW barrier, it was best to spin the cells CW first. We constructed a composite torque-speed relationship by combining data from different experiments. For CCW data, we examined each speed offset plot and drew a horizontal line through the first set of points (e.g., through the first four points in Fig. 14 *b*). This defined the speed-offset plateau. Then we drew a straight line through the descending set of points (e.g., through points 5 to 10, Fig. 14 *b*). The speed at the intersection of the second and first lines defined the plateau knee, and the point at which the descending line crossed the abscissa defined the 0-torque speed. Finally, if a second (minimum) torque plateau was encountered, we drew a horizontal line through the final set of points (e.g., the last two points in Fig. 14 *b*). The speed at the intersection of this line with the descending line defined the minimum-torque knee. We also projected the descending line back to the ordinate and noted its intercept. For CW data, we simply noted the maximum speed offset. The various speed offsets were converted to relative torques by dividing by the frequency at the speed-offset plateau (Eq. 5). Finally, we estimated the broken-motor CW speed (normalized to 100% on the low-power scale of the oscillator, assuming a high-to-low power ratio of 5), compared the slopes of the speed versus applied-torque lines (as in Fig. 9, ignoring the highest-speed CCW data), and recorded the CW/CCW ratio.

The cumulative data are summarized in Tables 1–4. Measurements at defined temperatures (Tables 1–3) were made with strain KAF95 in 40 mM TES (pH 7.0), 0.1 mM EDTA. Measurements at room temperature (Table 4) were made with strains KAF84 or KAF95 in either 1 mM potassium phosphate (pH 7.2), 0.1 mM EDTA or in the standard TES buffer.

The data of Tables 1–3 are summarized graphically in Fig. 16. Here, the points represent means and the error bars SEMs (the SD divided by the square root of the sample size). These data suggest the following: (*a*) Backward rotation is resisted by a steep barrier that yields, on average, at a torque about 2.2 times larger than the tethered-cell running torque. (*b*) Torque for forward rotation is constant up to a speed about 60% as large as the 0-torque speed. (*c*) At higher speeds, the torque drops linearly, falling below 0 and then leveling off at a negative torque (a torque that resists forward motion) about 1.7 times larger (in amplitude) than the tethered-cell running torque. (*d*) A linear fit to the descending part of this curve projects back to a zero-speed intercept at a torque about 2.8 times larger than the tethered-cell running torque. (*e*) The magnitude of the slope of this line decreases with temperature; therefore, zero-torque speeds increase with temperature. (*f*) Resistance to forward rotation can be overcome at very high speeds. (*g*) Broken cells spin at about 300 Hz when driven in a medium of conductivity 0.41 mS/cm at a field strength of about 16,000 V/cm. (*h*) If the motor is broken or de-energized, it is generally easier to spin the cell CW than CCW.

TABLE 1 Data obtained at 11.2°C

Quantity	Range	Mean	SD	Sample size*
Offset plateau (Hz)	6.6–16.1	9.9	2.7	28
Rel torque max	1.22–3.01	2.13	0.46	11
Rel torque intercept	1.47–4.54	2.74	0.75	28
−Rel torque min	0.74–2.67	1.72	0.54	22
Plateau knee (Hz)	29.0–83.0	56.4	13.3	28
0-torque speed (Hz)	64.8–126.0	92.5	13.8	28
Torque-min knee (Hz)	82.1–183.6	148.2	25.7	22
Broken speed CW (Hz)‡	153.3–366.2	256.0	58.6	24
Broken speed ratio (CW/CCW)	0.92–1.21	1.054	0.061	24

*Cells from two different cultures.

‡At 100% on the low-power scale.

TABLE 2 Data obtained at 16.2°C

Quantity	Range	Mean	SD	Sample size*
Offset plateau (Hz)	6.8–19.4	11.6	2.8	41
Rel torque max	1.27–4.31	2.36	0.72	29
Rel torque intercept	1.42–6.75	2.76	1.11	40
−Rel torque min	0.46–5.18	1.79	1.11	22
Plateau knee (Hz)	34.0–145.0	82.5	25.4	40
0-torque speed (Hz)	98.5–181.4	138.4	22.1	41
Torque-min knee (Hz)	159.8–300.6	231.0	39.8	21
Broken speed CW (Hz)‡	160.2–554.7	330.4	92.4	40
Broken speed ratio (CW/CCW)	0.94–1.42	1.073	0.078	40

*Cells from three different cultures.

‡At 100% on the low-power scale.

TABLE 3 Data obtained at 22.6°C

Quantity	Range	Mean	SD	Sample size*
Offset plateau (Hz)	7.8–15.6	11.1	2.1	20
Rel torque max	1.62–2.93	2.21	0.61	4
Rel torque intercept	2.02–4.96	3.25	0.88	20
−Rel torque min	0.67–3.07	1.56	0.68	18
Plateau knee (Hz)	112.9–326.1	193.8	53.7	20
0-torque speed (Hz)	220.5–409.0	286.9	53.6	20
Torque-min knee (Hz)	318.1–513.5	413.2	61.8	18
Broken speed CW (Hz)‡	207.0–492.2	313.1	69.5	20
Broken speed ratio (CW/CCW)	1.01–1.22	1.095	0.059	20

*Cells from one culture.

‡At 100% on the low-power scale.

TABLE 4 Data obtained at room temperature (~24°C)

Quantity	Range	Mean	SD	Sample size*
Offset plateau (Hz)	4.2–16.9	10.4	3.4	14
Rel torque max	1.38–3.40	2.29	0.54	11
Broken speed ratio (CW/CCW)	0.93–1.10	1.004	0.056	13

*Cells from four different cultures.

DISCUSSION

Electrorotation

This method has two major advantages: a tethered cell can be spun at very high speeds, and the applied torque does not depend on the orientation of the cell in the plane of the electrodes. The open design of our flow cell (Fig. 5) and the use of relatively heavy wire electrodes close to a thick sapphire window (Figs. 4, 5) ensured minimal heating (<0.2°C at the highest power levels utilized). Since a field rotating at 2.25 MHz executes 2250 cycles in 1 ms, it averages over cell orientations, even when cells are spun at 1 kHz. Also, it does not damage cell membranes.

Although it was not our intention to study electrorotation per se, we found that *E. coli* behaves as expected for the

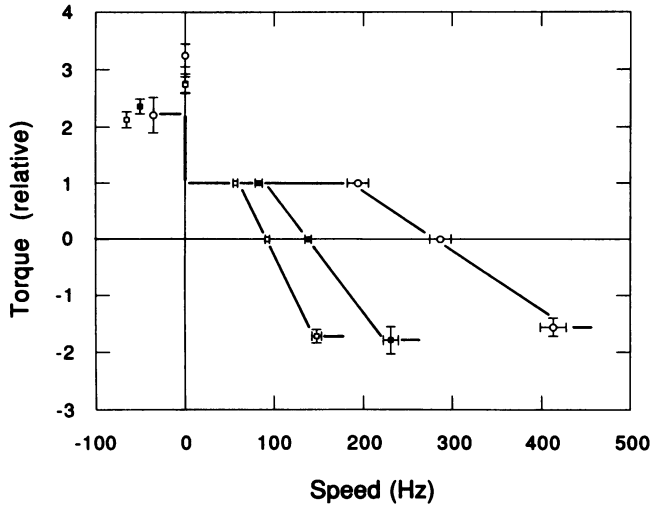

FIGURE 16 Relative torque as a function of speed for the data of Tables 1–3. □, 11.2°C (Table 1); ■, 16.2°C (Table 2); ○, 22.6°C (Table 3). Sign conventions as in Fig. 11. The error bars are SEs for the cell populations. The descending lines (as drawn) project from a common point on the ordinate at a relative torque of about 2.8. The extent to which these data are idealized can be judged by comparison with Figs. 11–15, which show results for individual cells.

simplest possible model: a spherical particle of (internal) dielectric constant ϵ_i and conductivity σ_i immersed in a liquid of (external) dielectric constant ϵ_e and conductivity σ_e; a shell model is not required. The external electric field polarizes the sphere, partly by dielectric polarization, partly by separation of free charge. This gives rise to a dipole field that rotates at the same rate and in the same direction as the applied electric field. However, due to the finite time required for redistribution of charges, which is on the order of ϵ/σ, the polarization dipole leads or lags the electric field vector. The applied torque is given by the cross product of these vectors. At low frequencies, the polarization dipole is in phase with the applied field, so the torque vanishes. At high frequencies, charges do not have time to redistribute during a rotation period, so the magnitude of the polarization dipole is small, and again the torque vanishes. Thus, the torque should be maximum at some intermediate frequency. The classical result, attributed to Lampa (1906), is quoted by Fuhr et al. (1986):

$$N = 3E^2r^3 \frac{\epsilon_e\sigma_i - \epsilon_i\sigma_e}{(2\epsilon_e + \epsilon_i)(2\sigma_e + \sigma_i)} \frac{\omega/\omega_0}{1 + (\omega/\omega_0)^2} \qquad (6)$$

with the maximum at

$$\omega_0 = \frac{4\pi(2\sigma_e + \sigma_i)}{2\epsilon_e + \epsilon_i}. \qquad (7)$$

Here, N is the torque, E is the amplitude of the applied electric field, r is the radius of the sphere, and ω is the angular frequency of the applied field (in cgs units). The magnitude of N is now believed to be larger by a factor $\epsilon_e = 80$ (Jones and Kallio, 1979; Sauer and Schlögl, 1985; Fuhr and Hagedorn, 1989). Our results are consistent with Eq. 6 provided that the dielectric constant of the cell is relatively high (about 600) and its conductivity is relatively low (about 0.4 mS/cm). These values are not far from those obtained by Fricke et al. (1956) from measurements of the electrical properties of suspensions of *E. coli.* Given values in this ballpark and $\epsilon_e = 80$, Eq. 6 predicts: (*a*) rotation of cells in the same direction as the applied field at low external conductivities but in the opposite direction at high external conductivities; (*b*) larger torques at high rather than at low external conductivities; and (*c*) zero torque at an external conductivity of about 0.05 mS/cm. All of these predictions are consistent with the data shown in Fig. 6. Eq. 6 also predicts: (*d*) maximum torque for $\sigma_e = 0.4$ mS/cm at a frequency of about 2.8 MHz, and (*e*) maximum torque for $\sigma_e = 0.004$ mS/cm at a frequency of about 0.94 MHz, both with a broad spectral response. These predictions are consistent with the data shown in Fig. 7. Finally, using the fact that the rotational frictional drag coefficient of a sphere of radius r is $8\pi\eta r^3$, where η is the viscosity of the external medium, Eq. 6 predicts a rotation rate in the standard TES buffer at 100% on the low-power scale of about 640 Hz. Even this is the right order of magnitude (without the factor ϵ_e, Tables 1–3). We do not know why the behavior of *E. coli*, a cell that is neither spherical nor a homogeneous isotropic dielectric, can be approximated by such a simple model. Perhaps its polarization is dominated by the displacement of free charge in the porous polyelectrolytic wall. Fuhr et al. (1992, Fig. 8) show a figure similar to our Fig. 7 for porous spheres of cellulose disulfate.

Torque as a function of speed

The procedure that we used to measure the speed offset (Eq. 4) or relative torque (Eq. 5) is based on the assumption that the frictional drag coefficient of a cell does not change when its motor is broken or de-energized. The justification for this assumption is based on the fact that similar speed-offset or relative-torque plots were obtained whether motors broke catastrophically (suddenly and completely; Figs. 12 *a*, 13 *a,b*), broke progressively (in a stepwise manner; Figs. 12 *b*, 14 *a,b,c*, 15 *a*), or were de-energized by brief treatment with an uncoupler (DNP or FCCP; Figs. 12 *c*, 15 *b*). This implies that drag arising from rotation-dependent proton pumping (if any) is relatively small at 0 proton motive force.

A steep increase in drag was noted during prolonged treatment with an uncoupler. Therefore, breaking the motor appears preferable to de-energizing it. All of the data used to construct Fig. 16 were obtained in this way. Washizu et al. (1993) "killed" cells with UV light; presumably, this de-energized them. If so, the final drag observed with this technique might depend on exposure.

We also discovered that cells with broken or de-energized motors were somewhat easier to turn CW than CCW (at low speeds, Fig. 9; Tables 1–4, last entry). Eisenbach et al. (1990) found that tethered wild-type cells tend to spin faster CW than CCW. This was due, in part, to the fact that cells going CCW pause or reverse briefly more often than cells going CW (Eisenbach, 1990). Another factor might be that tethered cells are easier to turn CW than CCW. This difference is due either to small direction-dependent changes in the orientation of a tethered cell or to differences in drag within the motor. The former seems more likely.

What about the motor torque-speed relationship? In the upper left and lower right quadrants of Fig. 16 (positive torque at negative speed or negative torque at positive speed, respectively) motor torque opposes externally applied torque. In either case, there is a limit to the amount of torque that the motor can deliver. At this limit, the motor either slips (delivers similar torque over a range of speeds, as in Fig. 15 *a*) or breaks (suddenly delivers substantially less torque, as in Fig. 13 *b*) or slips and then breaks (as in Fig. 12 *a*). The latter mode was the most common for CCW rotation (as in Fig. 14 *a*). Slippage can be reversible. For example, when the experiment of Fig. 10 (*closed symbols*) was repeated, we obtained identical results (noted in the legend). So one can cross the relative torque maximum (and presumably also the minimum; Tables 1–4) without permanently damaging the motor. Apparently, the motor yields, that is, is deformed enough to uncouple, and then returns to its native conformation. When the motor breaks catastrophically or completely, on the other hand, it is uncoupled irreversibly. However, as noted earlier, partial damage ascribable to individual force-generating elements can be repaired. Thus, we believe that the torque maxima and minima involve changes in motor structure not accounted for by models designed to describe its normal operating domain.

In the upper right quadrant of Fig. 16 (positive torque at positive speed) motor torque and externally applied torque act in parallel. This is the motor's normal operating domain. Torque remains constant up to a surprisingly high speed (roughly 60% of the 0-torque speed) and then drops linearly, crossing the 0-torque axis at the 0-torque speed. The descending line segments in this figure were all drawn from a common intercept on the 0-speed axis. The magnitude of the slope is smaller at higher temperatures. Other parameters of the fit appear to be temperature invariant.

The SEs shown in Fig. 16 are relatively small; however, the data sets were large and the variations from cell to cell were appreciable (Tables 1–3). For example, at 16.2°C the relative torque maximum was as high as 4.3 and the relative torque minimum was as low as −5.2 (Table 2). Therefore, the difference in amplitude between a relative torque maximum of about 2.2 and a relative torque minimum of about − 1.7 might not be significant (Fig. 16).

If the motor is tightly coupled, the data of Fig. 16 imply that it runs at constant efficiency over a considerable range of speeds. The power input is speed × protons per revolution × proton charge × proton motive force. With tight coupling at a fixed proton motive force, power input is directly proportional to speed. Power output is speed × torque. Therefore, the efficiency (power output divided by power input) is directly proportional to torque. Thus, it is constant up to the plateau knee and then drops linearly to zero at the 0-torque speed. For *Streptococcus*, the efficiency for tethered cells running under their own power was found to range between 0.5 and 0.9, while the efficiency for swimming cells was much lower, about 0.05 (both estimated with an uncertainty of a factor of 2) (Meister et al., 1987).

As far as we know, the proton motive force was fixed under the conditions of our experiments. The cells were in a motility medium rather than in a growth medium and at low density, equivalent to about 10^5 cells/ml, so aeration was adequate. For CW rotation, the motors broke at relatively small speeds, before protons could be pumped out of the cell at a substantial rate. *E. coli* is known to swim with its motors running near the 0-torque limit (Lowe et al., 1987). For CCW rotation, the torque leveled off at rotation rates only about twice as large. So, assuming tight coupling, the proton influx was equal to that of only two motors driving filaments in a bundle. Assuming a proton flux of 1240 per revolution (Meister et al., 1987), the influx at 400 Hz was about 5×10^5/s.

Our results are consistent with the data of Lowe et al. (1987) but not with their linear extrapolation. In those experiments, the viscous agent Ficoll was added to swimming cells of *Streptococcus* and *E. coli*, and body-roll and bundle frequencies were recorded. Motor torque was proportional to the product of the body-roll frequency and the viscosity of the medium, while motor frequency (speed) was equal to the sum of the body-roll and bundle frequencies. The torque rose linearly from a minimum value at a speed close to the 0-torque speed to a maximum value at a speed about half as large. These data were compared to those obtained at much lower speeds with tethered cells, "subject to considerable uncertainly, probably up to 40%." This uncertainty arose because the comparison depended on rotational frictional drag coefficients for both swimming and tethered cells and on the number of filaments per bundle, all of which were difficult to estimate. Our new results imply that the tethered-cell data should have been plotted about 40% lower relative to the swimming-cell data (Lowe et al., 1987, Fig. 3).

Our results agree with those of Washizu et al. (1993) in the CCW domain (constant torque up to about 100 Hz at room temperature) but not in the CW domain (constant torque up to about −100 Hz). Perhaps the motors that behaved in this way were partially damaged. Washizu et al. did encounter cells that stopped when driven CW, but they were not able to exclude the possibility that the angle of the tether changed, causing the cell bodies to adhere to the glass surface (S-I. Aizawa, private communication). As noted above following the discussion of Fig. 12, cells in our preparation that appeared to stop actually spun very slowly CW.

Iwazawa et al. (1993) studied the torque generated by tethered cells of a *cheY* deletion strain subjected to a low-frequency rotating electric field. They concluded that motor torque drops linearly from about −20 Hz to +55 Hz, confirming the extrapolation of Lowe et al. (1987). They did find that cells of small size were difficult to spin CW, so for this domain, they used large cells instead. Perhaps this allowed the motors of these cells to be more easily broken. In any event, our results are different.

Motor models

Rapidly rising torque at small negative speed is indicative of a tightly coupled ratchet mechanism, in which motion is allowed, either forward or backward, only when specific sites are protonated or deprotonated, so that passage of a fixed number of protons is required to carry the motor through one revolution. The motor does not have a fluid drive; one cannot force it backward without peril of breakage. In the model analyzed by Meister et al. (1989) a force-generating element can move forward provided that a proton-accepting site on the rotor in contact with a channel leading to the periplasm is protonated and an adjacent site in contact with a channel leading to the cytoplasm is not. If the membrane is fully energized, the joint probability for this is large, because the pH at the first site is smaller than its pK, and the pH at the second site is larger than its pK. For the element to move backward, the protonation must be the other way around, and the joint probability for this is small. Therefore, if one drives the cell backward with a torque that is large, but not so large that it overwhelms the normal constraints, the force-generating element will wait until the protonation becomes favorable and then move back one step. The larger the externally applied torque, the more difficult it becomes for the element to move forward, so the net backward rate increases. As noted earlier, we believe that the normal constraints are overwhelmed when the motor is driven backward or rapidly forward. The model of Meister et al. (1989) predicts speed limits, not torque limits.

Constant torque in the forward direction is more difficult to explain. In the model of Meister et al. (1989), the force-generating element is linked elastically to the rigid framework of the cell wall. At low speeds, one expects this linkage (the spring) to be stretched to equilibrium, so that the mechanical work done when it is stretched one more step is just balanced by the work that a proton can do on moving down its electrochemical gradient. With this mechanism, the force exerted by the spring is directly proportional to the proton motive force; it does not depend on the spring constant. But what if the displacement of the force-generating element were limited by a stop? Then the torque that can be generated is limited. When at the stop, there is not enough energy available for the element to take another step forward. When the element pulls away from the stop, the force exerted by the spring is smaller than the force at equilibrium. So such a motor, when running at low speed, will not exert a torque larger than some fixed value. The torque will remain constant up to a speed at which rates of proton translocation or of displacement of mechanical components are insufficient to keep the force-generating element near the stop. At higher speeds, the torque will drop linearly with speed, as before (Meister et al., 1989). This scenario was envisaged in the first embodiment of this model (Berg and Khan, 1983) to explain the saturation in speed with proton motive force observed for *E. coli* (Khan and Macnab, 1980a) and *Bacillus subtilis* (Khan and Macnab, 1980b; Shioi et al., 1980). However, it was abandoned when such saturation could not be demonstrated in studies of a motile *Streptococcus* (e.g., Meister and Berg, 1987). Recent studies suggest that saturation does not occur in this species (Khan et al., 1990). However, the idea of a stop suffers from at least one serious drawback: if the motor of a tethered cell running under its own power does not work close to equilibrium, why is the torque temperature independent (as observed for *Streptococcus*) (Khan and Berg, 1983)? With a stop, torque depends explicitly on the spring constant.

Note that when the motor is driven backward, it can deliver substantially higher torque, because the force-generating element is pushed against the stop by the externally applied torque, which is not limited by the energy available in proton transfer. The restoring force now depends primarily on the compliance of the stop.

A variety of other models exist. None, so far as we are aware, predict the results shown in Fig. 16. These models have been classified in various ways: according to the degree of coupling—tight, when the passage of fixed number of protons is required for each revolution, or loose, when the rotor can turn without proton transfer or protons can flow without motor rotation (Oosawa and Hayashi, 1986); according to the coupling mechanism—channel type, where the proton interacts simultaneously or sequentially with both stator and rotor components, or cross-bridge type, where the proton interacts only with the stator, which couples to the rotor in a conformation-dependent manner (Läuger and Kleutsch, 1990); or, finally, according to the way in which the force is generated—electrostatically, by direct coulomb interaction between diffusing protons and fixed charges (a better term is *electrodiffusively*), or indirectly, by conformational change or imposition of other chemical constraints (Berry, 1993). By these criteria, the model of Meister et al. (1989) is tightly coupled, channel type (although the channel complex acts like a cross bridge), and nonelectrodiffusive. These classifications are not mutually exclusive, and some models are not easy to categorize. Nevertheless, loosely coupled models and electrodiffusive models would appear to be ruled out by our data (Fig. 16). With such models, the torque is expected to rise smoothly from the lower right quadrant, through the upper right quadrant, and on into the upper left quadrant; there is no mechanism that strongly resists backward rotation.

Here, in approximate chronological order, are the models that have been proposed. In the initial arguments for flagellar rotation (Berg and Anderson, 1973) it was shown that three cross-bridges of the sort found in skeletal muscle, stepping 450 Hz, could power a flagellum spinning at 50 Hz. This calculation was made only to demonstrate the plausibility of a biological rotary motor. Later, when it was thought that the M ring is the rotor and the S ring the stator (but see Ueno et al., 1992), it was suggested that movement of one molecule down an electrochemical gradient (through the membrane) causes another molecule to exert a force on the S ring in a direction parallel to its face but normal to its radius (Berg, 1974). This idea was not very explicit. Adam (1977a,b) devised a loosely coupled mechanism in which motor rotation is driven by viscous streaming of the cytoplasmic membrane. Läuger (1977) suggested a mechanism in which protons move along a series of sites comprising two sets of ligands, one fixed to the rotor, the other to the stator, with the ligands of either kind arranged in intersecting rows (half-channels). In recent embodiments of this idea, the rows run along the surface of a cylinder at the periphery of the rotor (as also envisaged by Macnab, 1979) rather than along its face (Läuger, 1988, Model I), and the stator elements are elastically coupled to the cell wall (Kleutsch and Läuger, 1990). This model has been crafted to give the linear torque-speed relationship of Lowe et al. (1987); it does not show a steep barrier resisting backward rotation (cf. Kleutsch and Läuger, 1990, Fig. 17). Glagolev and Skulachev (1978; see also Glagolev, 1980) suggested an electrodiffusive model in which protonated amino groups on the rotor interact with deprotonated carboxyl groups on the stator (actually, within the cytoplasmic membrane); this model was not analyzed quantitatively. Mitchell (1984) expanded on this idea but also failed to develop it quantitatively. Berg et al. (1982) suggested a mechanism involving a proton motive redox loop that successively makes and breaks disulfide bonds linking the rotor to the stator. However, sulfhydryl reagents do not block flagellar rotation (Conley and Berg, 1984). Oosawa and Masai (1982) and Oosawa and Hayashi (1983) developed loosely coupled, cross-bridge-type mechanisms in which proton-accepting sites on the stator interact with sites on the rotor only when protonated, or with one set of sites on the rotor when protonated and with another set when not. In either case, the cross-bridges are able to move back and forth across the membrane whether protonated or not. These models do not show a steep barrier resisting backward rotation (cf. Oosawa and Hayashi, 1986, Fig. 6). As noted above, the model of Berg and Khan (1983) does show such a barrier (cf. Meister et al., 1989, Fig. 7). Macnab (1983) suggested that the motor might be able to work close to thermodynamic equilibrium, because energy is stored in the form of strained proton-motor bonds. Jou et al. (1986) considered an electrodiffusive cross-bridge model in which protonation triggers a phase transition with a finite lifetime; however, their analysis was limited to the demonstration of a threshold for rotation. Wagenknecht (1986) suggested a model in which twist-producing conformational changes in a rod at the base of the filament are generated by proton transfer; the rod is clamped by the stator at its proximal end during the power stroke and at its distal end during the recovery stroke. The dynamics of this model has not been worked out; however, it has the merit that it could resist externally applied torque. Läuger introduced a cross-bridge version of his earlier model in which a stator site is bound to the rotor when protonated, undergoing a conformational change that displaces the rotor and moves the proton across the membrane (Läuger, 1988, Model II). This model also has been crafted to give the linear torque-speed relationship of Lowe et al. (1987). Kobayasi (1988) developed a loosely coupled electrodiffusive model in which protons step along sites at the periphery of the rotor while interacting with negative fixed charges on the cytoplasmic side of the membrane. Fuhr and Hagedorn (1987, 1989) argued that the rotor might be driven by Quincke rotation (a variant of the mechanism used to spin tethered cells in which the electric field is constant; cf. Jones, 1984). This mechanism is loosely coupled, generates 0 torque at stall, and is autocatalytic, allowing the rotor to spin in either direction depending on the initial displacement. Also, it requires that the electric field be in the plane of the membrane. Murata et al. (1989) devised another loosely coupled electrodiffusive mechanism in which the force-generating sites are electrodes on the rotor charged at one rate and discharged at another, depending on their distance from opposing electrodes on the stator. This mechanism also generates 0 torque at stall and is autocatalytic (cf. Murata et al., 1989, Fig. 5). Blair (1990) described a chemically explicit, nearly tightly coupled electrodiffusive mechanism in which carboxyl groups on the rotor are protonated, pass a cluster of negative fixed charges on the stator, are depronated, and then are repelled. Berry (1993) developed a loosely coupled electrodiffusive model in which protons move through half-channels in the stator, intersecting with tilted lines of fixed charges on the rotor. This model produces a torque-speed relationship similar to that of Kleutsch and Läuger (cf. Berry, 1993, Fig. 8). Finally, two thermodynamic work cycles have been described in which a specific mechanism for force generation is not specified (Khan et al., 1990; Iwazawa et al., 1993; see also Yoshida et al., 1990). The first gives a torque-speed relationship that is more linear than the second; however, it is not clear that either predicts a steep barrier resisting CW rotation. The data summarized in Fig. 16 limit the field strongly.

Agenda

It is important to show that motors of *E. coli*, spinning under their own power, deliver nearly constant torque over a broad range of speeds. To that end, we have been measuring rotation rates of tethered minicells, cells that have relatively small frictional drag coefficients, as they are slowed by addition of viscous agents (K. A. Fahrner and H. C. Berg, manuscript in preparation). The preliminary results are consistent with the data of Fig. 16. It also is important to see whether *Streptococcus* shows a torque-speed relationship similar to that of *E. coli*. We began the present work with *Streptococcus*, but we found this species difficult to energize and tether in media of low conductivity. We hope that these problems can be overcome. More needs to be learned about the behavior of filaments in a bundle. If, say, six filaments turn CCW in synchrony in the bundle of a smoothly swimming cell, each driven by a motor delivering a relatively small torque (Lowe et al., 1987), then the rotation rate of the bundle must drop dramatically when one of the motors switches CW; its filament will strongly resist being driven backward. Presumably, this will cause the bundle to come apart; it might cause the cell to tumble. If not, the torque exerted by the remaining five motors, now turning more slowly, should be sufficient to break the first motor. Obviously, this does not occur. But, then, how are the filaments to form a new bundle? Must they all first spin CCW? There is no mechanism known to provide such coordination (cf. Macnab and Han, 1983; Ishihara et al., 1983). Food for thought.

We thank Karen Fahrner for preparation of strains, Win Hill for electronic design, Paul Horowitz for work on linear-graded filters, Markus Meister and Ed Purcell for discussions of electrodynamics, Don Rogers for help with fabrication of mechanical components, and Aravi Samuel for thoughts about motor models.

This work was supported by the Rowland Institute for Science and by grants AI-16478 from the National Institute of Allergy and Infectious Diseases and IBN-9341749 from the U.S. National Science Foundation.

REFERENCES

Adam, G. 1977a. Rotation of bacterial flagella as driven by cytoplasmic streaming. *J. Theor. Biol.* 65:713–726.

Adam, G. 1977b. Model of the bacterial flagellar motor: response to varying viscous load. *J. Mechanochem. Cell Motil.* 4:235–253.

Armstrong, J. B., J. Adler, and M. M. Dahl. 1967. Nonchemotactic mutants of *Escherichia coli. J. Bacteriol.* 93:390–398.

Berg, H. C. 1974. Dynamic properties of bacterial flagellar motors. *Nature (Lond.).* 249:77–79.

Berg, H. C., and R. A. Anderson. 1973. Bacteria swim by rotating their flagellar filaments. *Nature (Lond.).* 245:380–382.

Berg, H. C., and S. M. Block. 1984. A miniature flow cell designed for rapid exchange of media under high-power microscope objectives. *J. Gen. Microbiol.* 130:2915–2920.

Berg, H. C., and S. Khan. 1983. A model for the flagellar rotary motor. *In* Mobility and Recognition in Cell Biology. H. Sund and C. Veeger, editors. deGruyter, Berlin. 485–497.

Berg, H. C., M. D. Manson, and M. P. Conley. 1982. Dynamics and energetics of flagellar rotation in bacteria. *Soc. Exp. Biol. Symp.* 35:1–31.

Berry, R. M. 1993. Torque and switching in the bacterial flagellar motor: an electrostatic model. *Biophys. J.* 64:961–973.

Blair, D. F. 1990. The bacterial flagellar motor. *Semin. Cell Biol.* 1:75–85.

Blair, D. F., and H. C. Berg. 1988. Restoration of torque in defective flagellar motors. *Science (Washington DC).* 242:1678–1681.

Block, S. M., and H. C. Berg. 1984. Successive incorporation of force-generating units in the bacterial rotary motor. *Nature (Lond.).* 309: 470–472.

Block, S. M., D. F. Blair, and H. C. Berg. 1989. Compliance of bacterial flagella measured with optical tweezers. *Nature (Lond.).* 338:514–517.

Block, S. M., D. F. Blair, and H. C. Berg. 1991. Compliance of bacterial polyhooks measured with optical tweezers. *Cytometry.* 12:492–496.

Bradley, D. E. 1965. The preparation of specimen support films. *In* Techniques for Electron Microscopy. 2nd Edition. D. H. Kay, editor. F. A. Davis, Philadelphia. 68.

Conley, M. P., and H. C. Berg. 1984. Chemical modification of *Streptococcus* flagellar motors. *J. Bacteriol.* 158:832–843.

Eisenbach, M. 1990. Functions of the flagellar modes of rotation in bacterial motility and chemotaxis. *Mol. Microbiol.* 4:161–167.

Eisenbach, M., A. Wolf, M. Welch, S. R. Caplan, I. R. Lapidus, R. M. Macnab, H. Aloni, and O. Asher. 1990. Pausing, switching and speed fluctuation of the bacterial flagellar motor and their relation to motility and chemotaxis. *J. Mol. Biol.* 221:551–563.

Felle, H., D. L. Stetson, W. S. Long, and C. L. Slayman. 1978. Direct measurement of membrane potential and resistance in giant cells of *Escherichia coli. In* Frontiers of Biological Energetics. Vol. 2. P. L. Dutton, J. S. Leigh, and A. Scarpa, editors. Academic Press, New York. 1399–1407.

Foster, K. R., F. A. Sauer, and H. P. Schwan. 1992. Electrorotation and levitation of cells and colloidal particles. *Biophys. J.* 63:180–190.

Fricke, H., H. P. Schwan, K. Li, and V. Bryson. 1956. A dielectric study of the low-conductance surface membrane in *E. coli. Nature (Lond.).* 177:134–135.

Fuhr, G., and R. Hagedorn. 1987. Dielectric rotation—a principle in biological systems? *Stud. Biophys.* 121:25–36.

Fuhr, G., and R. Hagedorn. 1989. Dielectric motors—a new hypothesis for the bacterial flagella. *J. Theor. Biol.* 139:39–58.

Fuhr, G., R. Glaser, and R. Hagedorn. 1986. Rotation of dielectrics in a rotating electric high-frequency field: model experiments and theoretical explanation of the rotation effect of living cells. *Biophys. J.* 49:395–402.

Fuhr, G., W. M. Arnold, R. Hagedorn, T. Müller, W. Benecke, B. Wagner, and U. Zimmermann. 1992. Levitation, holding, and rotation of cells within traps made by high-frequency fields. *Biochim. Biophys. Acta.* 1108:215–223.

Glagolev, A. N. 1980. Reception of the energy level in bacterial taxis. *J. Theor. Biol.* 82:171–185.

Glagolev, A. N., and V. P. Skulachev. 1978. The proton pump is a molecular engine of motile bacteria. *Nature (Lond.).* 272:280–282.

Goodell, W. V., J. K. Coulter, and P. B. Johnson. 1973. Optical constants of Inconel alloy films. *J. Opt. Soc. Am.* 63:185–188.

Ishihara, A., J. E. Segall, S. M. Block, and H. C. Berg. 1983. Coordination of flagella on filamentous cells of *Escherichia coli. J. Bacteriol.* 155: 228–237.

Iwazawa, J., Y. Imae, and S. Kobayasi. 1993. Study of the torque of the bacterial flagellar motor using a rotating electric field. *Biophys. J.* 64: 925–933.

Jones, C. J., and S-I. Aizawa. 1991. The bacterial flagellum and flagellar motor: structure, assembly and function. *Adv. Microb. Physiol.* 32: 109–172.

Jones, T. B. 1984. Quincke rotation of spheres. *IEEE Trans. Ind. Applications.* IA-20:845–849.

Jones, T. B, and G. A. Kallio. 1979. Dielectrophoretic levitation of spheres and shells. *J. Electrostat.* 6:207–224.

Jou, D., C. Perez-Garcia, and J. E. Llebot. 1986. Bacterial flagellar rotation as a nonequilibrium phase transition. *J. Theor. Biol.* 122:453–458.

Khan, S., and H. C. Berg. 1983. Isotope and thermal effects in chemiosmotic coupling to the flagellar motor of *Streptococcus. Cell.* 32:913–919.

Khan, S., and R. M. Macnab. 1980a. The steady-state counterclockwise/clockwise ratio of bacterial flagellar motors is regulated by protonmotive force. *J. Mol. Biol.* 138:563–597.

Khan, S., and R. M. Macnab. 1980b. Proton chemical potential, proton electrical potential and bacterial motility. *J. Mol. Biol.* 138:599–614.

Khan, S., M. Dapice, and I. Humayun. 1990. Energy transduction in the bacterial flagellar motor: effects of load and pH. *Biophys. J.* 57:779–796.

Khan, S., M. Meister, and H. C. Berg. 1985. Constraints on flagellar rotation. *J. Mol. Biol.* 184:645–656.

Kleutsch, B., and Läuger, P. 1990. Coupling of proton flux and rotation in the bacterial flagellar motor: stochastic simulation of a microscopic model. *Eur. Biophys. J.* 18:175–191.

Kobayasi, S. 1988. Diffusion motor as a model of flagellar motor of bacteria. *Ferroelectrics.* 86:335–346.

Kobayasi, S., K. Maeda, and Y. Imae. 1977. Apparatus for detecting rate and direction of rotation of tethered bacterial cells. *Rev. Sci. Instrum.* 48:407–410.

Kuwajima, G. 1988. Construction of a minimum-size functional flagellin of *Escherichia coli. J. Bacteriol.* 170:3305–3309.

Lampa, A. 1906. Über rotationen im elektostatischen drehfelde. *Sitzungsber. Kaiserlichen Akad. Wiss.* 115(2a):1659–1690.

Läuger, P. 1977. Ion transport and rotation of bacterial flagella. *Nature (Lond.).* 268:360–362.

Läuger, P. 1988. Torque and rotation rate of the bacterial flagellar motor. *Biophys. J.* 53:53–65.

Läuger, P., and B. Kleutsch. 1990. Microscopic models of the bacterial flagellar motor. *Comments Theor. Biol.* 2:99–123.

Lowe, G., M. Meister, and H. C. Berg. 1987. Rapid rotation of flagellar bundles in swimming bacteria. *Nature (Lond.).* 325:637–640.

Macnab, R. M. 1979. How do flagella propel bacteria? *Trends Biochem. Sci.* 4:N10–N13.

Macnab, R. M. 1983. An entropy-driven engine—the bacterial flagellar motor. *In* Biological Structures and Coupled Flows. A. Oplatka and M. Balaban, editors. Academic Press, New York. 147–160.

Macnab, R. M. 1992. Genetics and biogenesis of bacterial flagella. *Annu.*

Rev. Genet. 26:131–158.

Macnab, R. M., and D. P. Han. 1983. Asynchronous switching of flagellar motors on a single bacterial cell. *Cell.* 32:109–117.

Maeda, K., Y. Imae, J-I. Shioi, and F. Oosawa. 1976. Effect of temperature on motility and chemotaxis of *Escherichia coli. J. Bacteriol.* 127: 1039–1046.

Manson, M. D., P. M. Tedesco, and H. C. Berg. 1980. Energetics of flagellar rotation in bacteria. *J. Mol. Biol.* 138:541–561.

Maurer, L., and P. E. Orndorff. 1987. Identification and characterization of genes determining receptor binding and pilus length of *Escherichia coli* type 1 pili. *J. Bacteriol.* 169:640–645.

Meister, M., and H. C. Berg. 1987. The stall torque of the bacterial flagellar motor. *Biophys. J.* 52:413–419.

Meister, M., G. Lowe, and H. C. Berg. 1987. The proton flux through the bacterial flagellar motor. *Cell.* 49:643–650.

Meister, M., S. R. Caplan, and H. C. Berg. 1989. Dynamics of a tightly coupled mechanism for flagellar rotation. *Biophys. J.* 55:905–914.

Mitchell, P. 1984. Bacterial flagellar motors and osmoelectric molecular rotation by an axially transmembrane well and turnstile mechanism. *FEBS Lett.* 176:287–294.

Murata, T., M. Yano, and H. Shimizu. 1989. A model for bacterial flagellar motor: free energy transduction and self-organization of rotational motion. *J. Theor. Biol.* 139:531–559.

Oosawa, F., and S. Hayashi. 1983. Coupling between flagellar motor rotation and proton flux in bacteria. *J. Physical Soc. Jpn.* 52:4019–4028.

Oosawa, F., and S. Hayashi. 1986. The loose coupling mechanism in molecular machines of living cells. *Adv. Biophys.* 22:151–183.

Oosawa, F., and J. Masai. 1982. Mechanism of flagellar motor rotation in bacteria. *J. Physical Soc. Jpn.* 51:631–641.

Ravid, S., and M. Eisenbach. 1984. Minimal requirements for rotation of bacterial flagella. *J. Bacteriol.* 158:1208–1210.

Sauer, F. A., and R. W. Schlögl. 1985. Torques exerted on cylinders and spheres by external electromagnetic fields: a contribution to the theory of field-induced cell rotation. *In* Interactions Between Electromagnetic Fields and Cells. A. Chiabrera, C. Nicolini, and H. P. Schwan, editors. Plenum Publishing Corporation, New York. 203–251.

Shimada, K., and H. C. Berg. 1987. Response of the flagellar rotary motor to abrupt changes in extracellular pH. *J. Mol. Biol.* 193:585–589.

Shioi, J-I., S. Matsuura, and Y. Imae. 1980. Quantitative measurements of proton motive force and motility in *Bacillus subtilis. J. Bacteriol.* 144: 891–897.

Silverman, M., and M. Simon. 1973. Genetic analysis of flagellar mutants in *Escherichia coli. J. Bacteriol.* 113:105–113.

Ueno, T., K. Oosawa, and S-I. Aizawa. 1992. M ring, S ring and proximal rod of the flagellar basal body of *Salmonella typhimurium* are composed of subunits of a single protein, FliF. *J. Mol. Biol.* 227:672–677.

Wagenknecht, T. 1986. A plausible mechanism for flagellar rotation in bacteria. *FEBS Lett.* 196:193–197.

Washizu, M., Y. Kurahashi, H. Iochi, O. Kurosawa, S-I. Aizawa, S. Kudo, Y. Magariyama, and H. Hotani. 1993. Dielectrophoretic measurement of bacterial motor characteristics. *IEEE Trans. Ind. Applications.* 29: 286–294.

Yoshida, S., S. Sugiyama, Y. Hojo, H. Tokuda, and Y. Imae. 1990. Intracellular Na^+ kinetically interferes with the rotation of the Na^+-driven flagellar motors of *Vibrio alginolyticus. J. Biol. Chem.* 265:20346–20350.